Two-path solid-state interferometry using ultra-subwavelength two-dimensional plasmonic waves

Kitty Y. M. Yeung,[1] Hosang Yoon,[1] William Andress,[1] Ken West,[2] Loren Pfeiffer,[2] and Donhee Ham[1,a)]
[1]*School of Engineering and Applied Sciences, Harvard University, 33 Oxford St., Cambridge, Massachusetts 02138, USA*
[2]*Department of Electrical Engineering, Princeton University, Princeton, New Jersey 08544, USA*

(Received 29 November 2012; accepted 20 December 2012; published online 14 January 2013)

We report an on-chip solid-state Mach-Zehnder interferometer operating on two-dimensional (2D) plasmonic waves at microwave frequencies. Two plasmonic paths are defined with GaAs/AlGaAs 2D electron gas 80 nm below a metallic gate. The gated 2D plasmonic waves achieve a velocity of $\sim c/300$ (c: free-space light speed). Due to this ultra-subwavelength confinement, the resolution of the 2D plasmonic interferometer is two orders of magnitude higher than that of its electromagnetic counterpart at a given frequency. This gigahertz proof-of-concept at cryogenic temperatures can be scaled to the terahertz–infrared range for room temperature operation, while maintaining the benefits of ultra-subwavelength confinement. © *2013 American Institute of Physics*.
[http://dx.doi.org/10.1063/1.4775668]

Plasmas appear in various forms in nature, with the collective electron density waves, or plasmonic waves, serving as a salient dynamic feature. Solid-state plasmas consisting of mobile electrons in metals and semiconductors are especially interesting, from the point of view that fabrication technologies available for solid-state materials allow us to design the boundaries and interfaces of the plasma media in order to engineer the plasmonic waves. In particular, surface plasmons on three-dimensional (3D) bulk metals have been an active subject of research in photonics. One of these efforts with surface plasmons concerns developing interferometers.[1–4] A prominent advantage of surface plasmonic interferometers is their high resolution. Surface plasmons can achieve a velocity as low as $\sim c/10$ (c: free-space light speed) with a proportionally reduced wavelength.[5] This subwavelength confinement makes surface plasmon interferometers more sensitive to the path length difference and the surrounding dielectric media, leading to the higher resolution in measurements of physical quantities such as length and dielectric constant.

While surface plasmons on 3D bulk metals typically appear in the optics regime, plasmonic waves in 2D conductors, such as GaAs/AlGaAs 2D electron gas (2DEG) and graphene, can appear in the gigahertz (GHz)–terahertz (THz) and infrared frequencies.[6–12] These 2D plasmons exhibit a greater subwavelength confinement with velocities far below[10] $\sim c/100$. Harnessing this ultra-subwavelength confinement, we develop a high-resolution 2D plasmonic interferometer at microwave frequencies in the electronics regime, drawing a parallel line of development to surface plasmonic interferometers in photonics.

For proof of concept, we use GaAs/AlGaAs 2DEG as a 2D plasmonic medium and construct a Mach-Zehnder interferometer, whose two paths are defined by mesa-etching the 2DEG[13] (Fig. 1). The curved 2DEG path has a length of $l_1 \sim 191\ \mu$m and the linear path has a length of $l_2 \sim 120\ \mu$m while both have the same width of $w \sim 8\ \mu$m. The left metallic coplanar waveguide (CPW)[14] consisting of a signal line ("S") and two ground lines ("G") guides an electromagnetic wave onto the left end of the interferometer; the CPW's signal line makes an Ni/Au/Ge ohmic contact to the 2DEG. The excited plasmonic wave splits into two plasmonic waves along the two 2DEG paths, which superpose at the right end of the interferometer. By this junction, the two waves develop a frequency-dependent phase difference due to the path length difference; thus, their superposition exhibits an interference pattern with frequency. This superposed wave excites an electromagnetic wave onto the right CPW, which we measure to study the interference. The characteristic impedance, Z_0, of both CPWs is designed to be 50 Ω.

A metallic top gate placed 80 nm above both 2DEG paths serves as an *ac* plasmonic ground (Fig. 1); each 2DEG

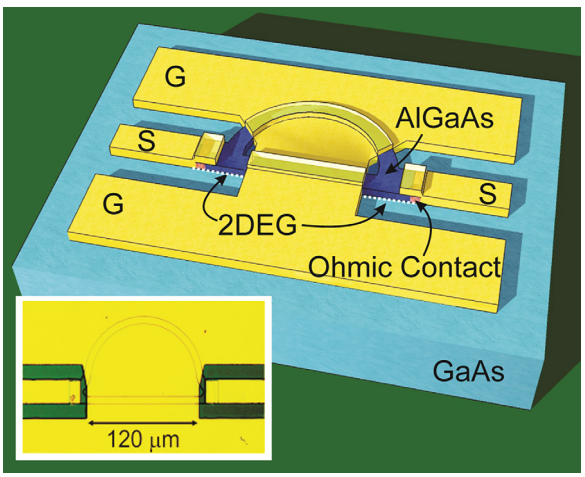

FIG. 1. Diagram of the 2D plasmonic Mach-Zehnder interferometer (not drawn to scale). The inset shows an optical image of an actual implementation. 2DEG forms between AlGaAs and GaAs layers.

a)Author to whom correspondence should be addressed. Electronic mail: donhee@seas.harvard.edu.

signal path with the gate as the *ac* ground then forms a plasmonic transmission line.[10] The plasmonic ground is merged with the CPWs' ground lines. This ground sharing ensures seamless continuation of the purely plasmonic transmission lines from the purely electromagnetic CPWs;[10] with no such ground sharing, the gate itself would act as an electromagnetic path, instead of a plasmonic ground. The gate also serves to further slow the 2D plasmonic velocity (which is already small due to the reduced dimensionality) by shortening the Coulomb interaction range within 2DEG.[10,15] This further enhances subwavelength confinement and interferometer resolution. The gated 2D plasmonic velocity,[15] $v_p = \sqrt{(ne^2d)/(m^*\kappa\varepsilon_0)}$, is $\sim c/300$ in our case as seen shortly (n: conduction electron density per unit area; m^*: effective electron mass; d: 2DEG-gate distance; κ: dielectric constant of the AlGaAs medium between the 2DEG and gate). Yet another role of the gate is to provide a *dc* bias to tune the electron density, hence v_p. In actuality, we apply to the CPWs' signal lines a *dc* bias with reference to the ground lines, so that the gate is effectively biased in the opposite polarity relative to the 2DEG.

We perform microwave scattering experiments[13] in the dark up to 50 GHz with a vector network analyzer to obtain frequency-domain interference patterns. Temperature is at 4.2 K so that plasmonic dynamics is not masked by electron scatterings. The raw s-parameters contain not only the interferometer effect but the effect of direct coupling between the left and right on-chip CPWs bypassing the interferometer. This parasitic coupling is separately measured and de-embedded,[10,11,13] yielding s-parameters containing only the interferometer effect. The s-parameters discussed from here on are such de-embedded ones, unless otherwise stated. Theoretically, the transmission s_{21} of the interferometer can be approximated as the following, where we safely consider only the 1st-order signal pathways, and for simplicity neglect the ohmic contacts and the short ungated 2DEG regions (Fig. 1)[13]

$$s_{21} \approx \frac{4Z_0Z}{(Z+2Z_0)^2}\left[e^{-\alpha l_1}e^{-i\beta l_1} + e^{-\alpha l_2}e^{-i\beta l_2}\right] = \frac{4Z_0Z}{(Z+2Z_0)^2}A_1e^{-i\beta l_1}\left[1+\frac{A_2}{A_1}e^{-i\Delta\phi}\right]. \quad (1)$$

Z is the identical characteristic impedance of the either plasmonic line;[13] $\beta \equiv \omega/v_p$ and α are the wavenumber and attenuation constant (the latter due to electron scatterings in 2DEG) of the plasmonic lines; $A_1 \equiv e^{-\alpha l_1}$ and $A_2 \equiv e^{-\alpha l_2}$; and $\Delta\phi \equiv \beta(l_1 - l_2) = \omega(l_1 - l_2)/v_p$ is the phase difference between the two plasmonic waves at the right junction of the interferometer. The s_{21} is proportional to the superposition of the two plasmonic waves and will exhibit an interference pattern with frequency. The factor $4Z_0Z/(Z+2Z_0)^2 \equiv F$ is complex in general, as Z is generally complex due to loss caused by electron scatterings; however, F exhibits a practically constant magnitude and a negligible phase over the measurement frequency range.[13]

Figure 2(a) shows the magnitude of the measured s_{21} vs. frequency at various effective gate biases. At each bias, the s_{21} magnitude shows the anticipated interference pattern with

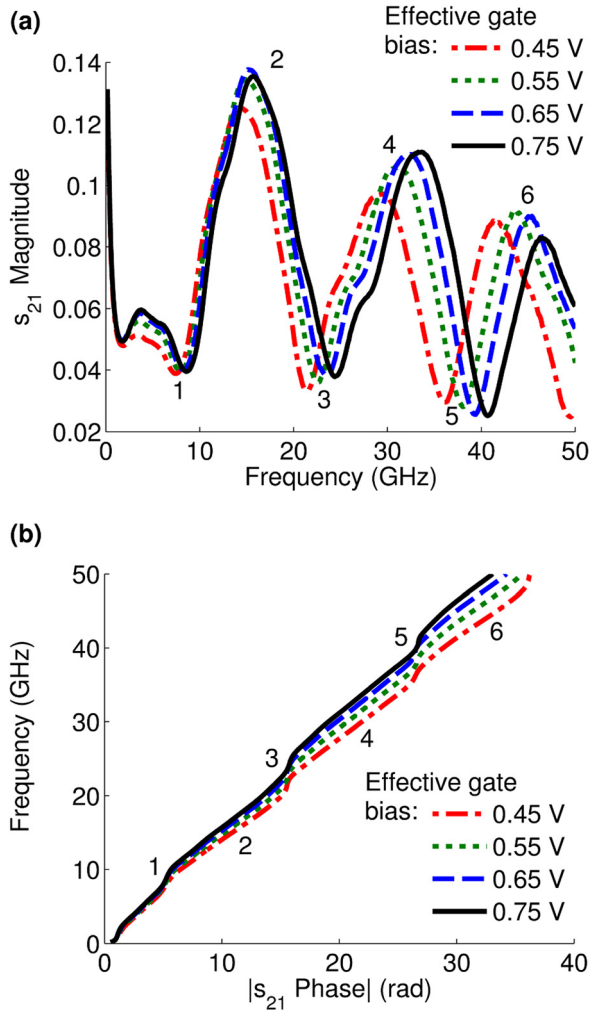

FIG. 2. (a) s_{21} magnitude; (b) absolute value of s_{21} phase at effective gate bias 0.45 V (red, semi-dashed), 0.55 V (green, dotted), 0.65 V (blue, dashed), and 0.75 V (black, solid). Temperature: 4.2 K. In (b), y-axis is frequency and x-axis is s_{21} phase, following the convention of showing dispersion.

destructive dips marked as 1, 3, and 5, and constructive peaks as 2, 4, and 6. The reduction of the peak and dip magnitudes with frequency, which is not predicted by Eq. (1), stems from the frequency dependent behaviors of the ohmic contacts and the ungated 2DEG regions.[10] According to Eq. (1), the destructive dips (constructive peaks) with amplitudes proportional to $1-(+)$ A_2/A_1 occur at frequencies that make $\Delta\phi \equiv \omega(l_1 - l_2)/v_p$ odd (even) integer multiples of π. The increasing gate bias increases v_p, leading to the shift of the interference pattern to the right [Fig. 2(a)]; for a larger v_p, higher frequencies are required to produce the same $\Delta\phi$. From these considerations in connection with Eq. (1), we can extract, at a given bias, v_p at six different frequencies corresponding to the three dips and three peaks of the s_{21} magnitude. Figure 3 shows the range (red bar) and median (red square) of such six extracted v_p values at each bias, where the median is the average of the two middle v_p values. While v_p must be constant at a given bias, the extracted v_p shows the frequency variation (bar). This is due to the frequency-dependent behaviors of the ohmic contacts and ungated 2DEG regions,[10] which can shift the dip and peak positions from the ideal positions predicted by Eq. (1). While the actual v_p should monotonically increase with gate bias, the extracted v_p shows deviation from this

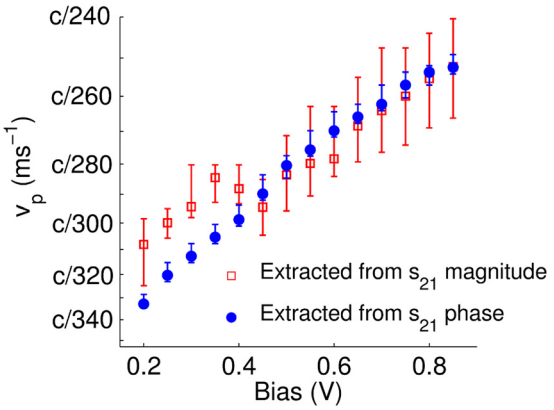

FIG. 3. The plasmonic velocities extracted from the measured s_{21} magnitude (red squares and bars) and those extracted from the measured s_{21} phase (blue dots and bars). The squares/dots and bars, respectively, represent the median values and frequency-dependent variations at given biases.

trend at biases below 0.4 V (Fig. 3). We suspect that this abnormality is also caused by the ohmic contacts, this time through their substantial bias dependency below 0.4 V, which considerably affects the magnitude of s_{21}.

We alternatively extract v_p from the phase, θ, of the measured s_{21}, whose absolute value vs. frequency is shown in Fig. 2(b) at various biases. Equation (1) yields the following expression for θ (as stated earlier, $4Z_0Z/(Z+2Z_0)^2$ of Eq. (1) has a negligible phase):

$$\theta = -\arctan\left[\frac{\sin(l_1\omega/v_p) + (A_2/A_1)\sin(l_2\omega/v_p)}{\cos(l_1\omega/v_p) + (A_2/A_1)\cos(l_2\omega/v_p)}\right], \quad (2)$$

which reduces to $\theta = \omega(l_1+l_2)/(2v_p)$ for $A_1 = A_2$, as expected. Equation (2) predicts that with a larger bias, thus with a larger v_p, θ increases more slowly with frequency, as evident in Fig. 2(b). We extract v_p by fitting Eq. (2) to Fig. 2(b) at each gate bias. The A_2/A_1 ratios required for this fitting are extracted from the amplitudes of the dips and peaks of the s_{21} magnitude in connection with Eq. (1); specifically, at a given bias, a total of five A_2/A_1 ratios are obtained over five frequency ranges, with each range spanning from a dip to its adjacent peak;[13] while the actual A_2/A_1 ratio must be constant at a given bias, the variations of the extracted A_2/A_1 values with frequencies at a given bias are caused by the frequency-dependent effects of the ohmic contacts and ungated 2DEG regions. Subsequently, fitting of Eq. (2) to Fig. 2(b) is performed in each of these five frequency ranges, yielding five values of v_p at each bias. The ranges (blue bars) and medians (blue dots) of v_p so extracted from the measured s_{21} phase are shown in Fig. 3. As compared to v_p extracted from the s_{21} magnitude, this s_{21}-phase based extraction shows a greater immunity to the ohmic contact and ungated 2DEG effects: first, the frequency-dependent variation (sizes of the bars) is smaller; second, v_p shows the expected monotonic increase with an increasing bias even below 0.4 V. At biases in excess of 0.4 V, the median values of v_p extracted from the s_{21} magnitude and those extracted from the s_{21} phase show a match within 5%. The high-fidelity v_p extracted from s_{21} phase ranges from $\sim c/330$ (0.2 V) to $\sim c/250$ (0.85 V), attesting to ultra-subwavelength confinement of the gated 2D plasmons.

We further confirm the plasmonic interferences by temperature-dependent measurements. As temperature rises, the electron scatterings are promoted to increase the ohmic resistance,[16] degrading the 2DEG as a plasmonic medium. Quantitatively, while the plasmonic quality factor, $Q = \omega\tau$ (τ: mean electron scattering time), is greater than unity at 4.2 K at GHz frequencies, τ and thus Q decreases with temperature, making the observation of plasmonic waves and their interferences increasingly difficult. This is attested by temperature-dependent measurements of Fig. 4, where we show, for a reason that will be clear shortly, raw s_{21}-parameters without de-embedding the direct coupling between the two CPWs. As temperature rises towards 40 K, the s_{21} magnitude gradually decreases, blurring the interference pattern [Fig. 4(a)]. At room temperature, the ohmic resistance becomes so high that the interferometer becomes effectively open-circuited; the non-zero raw s_{21} magnitude at room temperature in Fig. 4(a) is due to the direct coupling between the CPWs. This is confirmed by the close similarity between this raw s_{21} magnitude at room temperature and the s_{21} magnitude of the actual open device at 4.2 K, where this open device is attained by biasing the gate at −0.4 V and depleting the 2DEG.[13] It is for this comparison that Fig. 4 presents raw s-parameters. The raw s_{21} phase in Fig. 4(b) tells the same physics: up to 40 K, s_{21} phase does not change appreciably, as the plasmonic wave, while increasingly masked by electron scatterings, observably

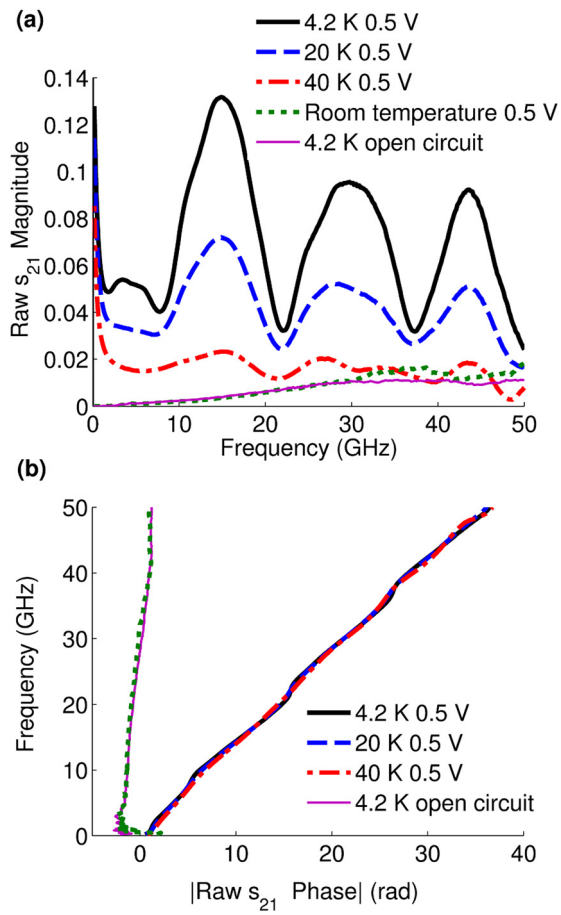

FIG. 4. (a) Magnitude and (b) phase of the interferometer's raw s_{21} parameters at 4.2 K (black, solid), 20 K (blue, dashed), 40 K (red, semi-dashed), and room temperature (green, dotted), and of the actual open circuits' s_{21} parameters at 4.2 K (magenta, thin).

maintains the same velocity. At room temperature, the plasmonic dynamics is completely masked, and the interferometer behaves as an open circuit.

Due to the ultra-subwavelength confinement of 2D plasmons ($v_p \sim c/300$), the interferometer achieves a high resolution. Since $\Delta\phi \equiv \omega(l_1 - l_2)/v_p$ and $v_p \sim c/300$, a given path length difference, $l_1 - l_2$, will lead to a $\sim 300/\sqrt{\kappa_{EM}}$ times larger phase difference in the plasmonic interferometer than in an electromagnetic wave interferometer whose wave speed is $c/\sqrt{\kappa_{EM}}$ (κ_{EM} is the effective dielectric constant of the medium in the electromagnetic interferometer). So for the given $\Delta\phi$ resolution of the vector network analyzer, the plasmonic interferometer achieves a $\sim 300/\sqrt{\kappa_{EM}}$ times higher resolution than the electromagnetic interferometer at the same frequency. The plasmonic interferometer is also capable of a higher resolution detection of changes in the physical parameters on which v_p depends, where this benefit is again attributed to the ultra-subwavelength confinement. For example, a change in the refractive index $\sqrt{\kappa}$ of the medium separating the gate and the 2DEG incurs a change in $\Delta\phi$ as $d(\Delta\phi)/d\sqrt{\kappa} = [\omega(l_1 - l_2)/c] \times [c/(v_p\sqrt{\kappa})]$, while this derivative for an electromagnetic interferometer with a wave speed of $c/\sqrt{\kappa_{EM}}$ is[17] $d(\Delta\phi)/d\sqrt{\kappa_{EM}} = \omega(l_1 - l_2)/c$. Thus, the plasmonic interferometer is $\sim 300/\sqrt{\kappa}$ times more sensitive to the refractive index change, achieving a higher resolution by the same factor. The plasmonic interferometer can also detect the changes in the 2DEG electron density, n, and the effective electron mass, m^*, with high resolution, as v_p depends on these quantities. They are quantities irrelevant to electromagnetic interferometers; thus, their detection is a bonus feature of our interferometer.

Despite the high-resolution advantage, the GHz proof-of-concept prototype presented in this paper is limited to cryogenic operation. At higher THz and infrared frequencies, 2D plasmons in GaAs/AlGaAs 2DEG and graphene can be observed at room temperature,[12,18] while maintaining the nature of subwavelength confinement. Scaling our design into this higher frequency regime[13] may enable high-resolution THz and infrared interferometric applications, such as biochemical detection, molecular spectroscopy, and precision modulation, at room temperature.

This work was supported by the Air Force Office of Scientific Research under Contract Number FA 9550-09-1-0369. Device fabrication was performed in part at the Center for Nanoscale Systems at Harvard University.

[1]H. F. Schouten, N. Kuzmin, G. Dubois, T. D. Visser, G. Gbur, P. F. A. Alkemade, H. Blok, G. W.'t Hooft, D. Lenstra, and E. R. Eliel, Phys. Rev. Lett. **94**, 053901 (2005).
[2]R. Zia and M. L. Brongersma, Nat. Nanotechnol. **2**, 426 (2007).
[3]S. I. Bozhevolnyi, V. S. Volkov, E. Devaux, J.-Y. Laluet, and T. W. Ebbesen, Nature **440**, 508 (2006).
[4]J. Feng, V. S. Siu, A. Roelke, V. Mehta, S. Y. Rhieu, G. T. R. Palmore, and D. Pacifici, Nano Lett. **12**, 602 (2012).
[5]W. L. Barnes, A. Dereux, and T. W. Ebbesen, Nature **424**, 824 (2003).
[6]F. Stern, Phys. Rev. Lett. **18**, 546 (1967).
[7]S. J. Allen, Jr., D. C. Tsui, and R. A. Logan, Phys. Rev. Lett. **38**, 980 (1977).
[8]I. V. Kukushkin, J. H. Smet, S. A. Mikhailov, D. V. Kulakovskii, K. von Klitzing, and W. Wegscheider, Phys. Rev. Lett. **90**, 156801 (2003).
[9]P. J. Burke, I. B. Spielman, J. P. Eisenstein, L. N. Pfeiffer, and K. W. West, Appl. Phys. Lett. **76**, 745 (2000).
[10]W. F. Andress, H. Yoon, K. Y. M. Yeung, L. Qin, K. West, L. Pfeiffer, and D. Ham, Nano Lett. **12**, 2272 (2012).
[11]H. Yoon, K. Y. M. Yeung, V. Umansky, and D. Ham, Nature **488**, 65 (2012).
[12]L. Ju, B. Geng, J. Horng, C. Girit, M. Martin, Z. Hao, H. A. Bechtel, Z. Liang, A. Zettl, Y. R. Shen, and F. Wang, Nat. Nanotechnol. **6**, 630 (2011).
[13]See supplementary material at http://dx.doi.org/10.1063/1.4775668 for materials, fabrication, detailed measurements, physical properties, derivation of Eq. (1), and the scaling behavior.
[14]W. F. Andress and D. Ham, IEEE J. Solid-State Circuits **40**, 638 (2005).
[15]A. Eguiluz, T. K. Lee, J. J. Quinn, and K. W. Chiu, Phys. Rev. B **11**, 4989 (1975).
[16]B. J. F. Lin, D. C. Tsui, M. A. Paalanen, and A. C. Gossard, Appl. Phys. Lett. **45**, 695 (1984).
[17]R. Ince and R. Narayanaswamy, Anal. Chim. Acta **569**, 1 (2006).
[18]Y. M. Meziani, H. Handa, W. Knap, T. Otsuji, E. Sano, V. V. Popov, G. M. Tsymbalov, D. Coquillat, and F. Teppe, Appl. Phys. Lett. **92**, 201108 (2008).